**J. Cent. South Univ.** (2025) 32: 3203−3219
**DOI:** https://doi.org/10.1007/s11771-025-5999-y

Springer

Research Article

# Stress corrosion cracking behavior of TIG welded Al-Mg-Mn-Sc-Zr alloy

TANG Zhong-qin(唐中琴)[1], JIANG Feng(姜锋)[2, 3]*, LONG Meng-jun(龙梦君)[2],
YE Peng-cheng(叶鹏程)[2], WU Ming-jin(吴明锦)[3]

1. School of Minerals Processing and Bioengineering, Central South University, Changsha 410083, China;
2. School of Materials Science and Engineering, Central South University, Changsha 410083, China;
3. Light Alloy Research Institute, Central South University, Changsha 410083, China



**Abstract:** Al-Mg-Mn-Sc-Zr alloys with excellent weldability have emerged as ideal candidates for aerospace applications. Currently, the investigations on the corrosion behavior of alloys under tungsten inert gas (TIG) welding conditions are insufficient. Here, the stress corrosion cracking (SCC) behavior of base metal (BM) and weld zone (WZ) of TIG welded Al-Mg-Mn-Sc-Zr alloys was investigated by using pre-cracked compact tensile samples immersed in 3.5% NaCl solution. The direct current potential drop (DCPD) method was used to record the crack propagation. The microstructure and fracture morphology of different regions of TIG welded joints were studied by SEM, EBSD and TEM, and the SCC crack propagation mechanism of BM and WZ was analyzed. The results demonstrated that the critical stress intensity factor for stress corrosion cracking ($K_{ISCC}$) of BM and WZ was 7.05 MPa·m$^{1/2}$ and 11.79 MPa·m$^{1/2}$, respectively. Then, the crack propagation rate of BM was faster than that of WZ, and BM was more susceptible to SCC than WZ. Additionally, the fracture mode of the BM mainly exhibited transgranular fracture, while the fracture mode of the WZ mainly exhibited intergranular and transgranular mixed fracture. Moreover, SCC crack propagation was attributed to the combined effect of anodic dissolution and hydrogen embrittlement. This study will provide experimental and theoretical basis for the wide application of TIG welded Al-Mg-Mn-Sc-Zr alloys in aerospace.

**Key words:** tungsten inert gas (TIG) welded Al-Mg-Mn-Sc-Zr alloy; stress corrosion cracking (SCC); critical stress intensity factor ($K_{ISCC}$); direct current potential drop (DCPD)

**Cite this article as:** TANG Zhong-qin, JIANG Feng, LONG Meng-jun, YE Peng-cheng, WU Ming-jin. Stress corrosion cracking behavior of TIG welded Al-Mg-Mn-Sc-Zr alloy [J]. Journal of Central South University, 2025, 32(9): 3203−3219. DOI: https://doi.org/10.1007/s11771-025-5999-y.

## 1 Introduction

Non-heat treatable Al-Mg alloys with a magnesium content of 1%−6% have been used in welded structures for a long time. Due to their good weldability [1], it is possible to produce welded joints free of cracks and pores [2]. Compared with heat-treatable aluminum alloys, Al-Mg alloys are medium strength alloys. Studies have shown that the progress of microalloying processing has greatly improved the mechanical properties and corrosion resistance of Al-Mg alloys, especially the addition of Sc element that can significantly improve the strength and toughness of Al-Mg alloys [3−10]. The widespread use of Al-Mg alloys is inseparable from reliable welding methods through which components of different sizes and geometries can be fabricated. So far, many welding methods such as tungsten inert gas (TIG) welding, laser beam

**Foundation item:** Project(2023GK1080) supported by the Major Special Projects of Hunan Province of China
**Received date:** 2024-03-03; **Accepted date:** 2025-03-19
**Corresponding author:** JIANG Feng, PhD, Professor; E-mail: jfeng2@csu.edu.cn; ORCID: https://orcid.org/0000-0003-0239-259X

welding (LBW), electron beam welding (EBW), and friction stir welding (FSW) have been applied to the welding of aluminum alloys [11−15]. TIG welding is a traditional technique for welding aluminum alloys and is often used to join high-precision components in various industries (automotive, aerospace, etc.) [16]. The method has the advantages of low cost, flexible operation, good welding quality, and stable process, so it is widely used in the welding of Al-Mg alloys [17].

Currently, a lot of research is devoted to the microstructure and mechanical properties of TIG-welded Al-Mg alloys [18−20]. MENZEMER et al [21] found that the microstructure of the fusion zone was significantly coarsened due to the relatively slow heat dissipation during TIG welding. YANG et al [22] found that the primary $Al_3Er$ phase and secondary $Al_3Er$ played an important role in the refinement and strengthening of the fusion zone during TIG welding. SUBBAIAH [23] welded Al-Mg-Mn-Sc-Zr cast alloys using TIG welding, and the microstructure and mechanical properties of the welded joints were examined and analyzed. The results clearly showed that numerous fine $Al_3Sc$ particles were uniformly distributed in the aluminum matrix, eliminating the original casting voids in the weld. BABU et al [24] conducted TIG welding of 4 mm marine aluminum alloy AA5083 and found that the filler rod containing Sc could significantly improve the tensile properties of the alloy welded joints. Besides, XU et al [25] investigated the microstructure and mechanical properties of 2-mm-thick Al-Mg-Sc-Zr alloy TIG welded joints. The results showed that the excellent mechanical properties of TIG welded joints were mainly attributed to the Orowan strengthening and grain boundary strengthening induced by $Al_3$(Sc, Zr) nanoparticles. However, there is no literature related to stress corrosion cracking (SCC) of 20-mm-thick Al-Mg-Mn-Sc-Zr alloy TIG welded joints. SCC is a cause of premature failure in various strategic industries such as aerospace. Therefore, it is of great significance to study the SCC of Al-Mg-Mn-Sc-Zr alloy TIG welded joints. Prominently, the direct current potential drop (DCPD) method is widely used in the study of SCC crack propagation due to its good repeatability and high sensitivity [26].

In this study, 20-mm-thick Al-Mg-Mn-Sc-Zr alloy hot-rolled plates were welded by the TIG welding process using Al-Mg-Sc matching welding wire. The SCC behavior of TIG welded Al-Mg-Mn-Sc-Zr alloy BM and WZ was studied by combining the microstructure of the welded joints and using the DCPD method to measure crack propagation. The critical stress intensity factor for stress corrosion cracking ($K_{ISCC}$) of the BM and WZ in 3.5% NaCl solution were tested, and the SCC crack propagation mechanism was explored.

## 2 Materials and methods

### 2.1 Materials and sample preparation

The base metal (BM) used in the TIG welding experiment was an Al-Mg-Mn-Sc-Zr hot-rolled plate with a thickness of 20 mm, and the welding wire was an Al-Mg-Sc alloy welding wire. The stress corrosion properties of TIG welded joints were investigated after welding. The composition (mass fraction, wt.%) of BM and welding wire is shown in Table 1. The schematic diagram of the TIG welded joints of Al-Mg-Mn-Sc-Zr alloys and the sample cutting positions are shown in Figure 1, where L, T and S represent the longitudinal (rolling direction), transverse and short transverse directions of Al-Mg-Mn-Sc-Zr sheet, respectively.

**Table 1** Main chemical composition of BM and welding wire wt.%

| Material | Mg | Mn | Sc | Zr | Al |
|---|---|---|---|---|---|
| BM | 6.04 | 0.31 | 0.25 | 0.10 | Balance |
| Welding wire | 6.68 | 0.32 | 0.35 | 0.15 | Balance |

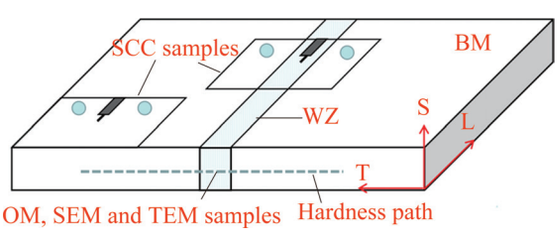


**Figure 1** Schematic diagram of sampling direction and microstructure observation direction of Al-Mg-Mn-Sc-Zr TIG welded joint (WZ represents the weld zone)

### 2.2 Microstructure characterization

The corrosion morphologies, secondary phase particles, and tensile fracture morphologies of the samples were observed using a scanning electron

microscope (SEM) (FEI-Quanta 200, Helios Nanolab 600i, JEOL JSM-7900F and FEI-Sirion 200) equipped with energy-dispersive X-ray spectroscope (EDS). Moreover, the microstructure of the samples was analyzed under a Tecnai G2 F20 transmission electron microscope (TEM) operated at 200 kV.

The SCC crack propagation morphologies of BM and WZ were analyzed by operating a JEOL JSM-7900F scanning electron microscope equipped with an EBSD detector at 15 kV. The BM and WZ samples after the SCC test were polished with SiC sandpaper, metallographic sandpaper, and diamond suspension in turn, and finally electropolished with electrolytic polishing solution (perchloric acid 10 mL + ethanol 90 mL). The polishing voltage and polishing time were 16.1 V and 15 s, respectively. After scanning, the results were analyzed using Channel 5 software.

### 2.3 Microhardness distribution

Figure 2 shows the microhardness distribution of TIG welded joints of 20-mm-thick Al-Mg-Mn-Sc-Zr alloy hot-rolled sheets. Obviously, the hardness profile was symmetrical concerning the weld centerline. From the center of the weld to the BM, the microhardness gradually increased, and the lowest hardness was obtained at the center of the weld. The hardness in the center of the weld seam of the welded joint was about 77HV, and the hardness value was the highest in the BM, reaching 115HV. Moreover, the welded joint was sequentially divided into 4 typical zones: weld zone (WZ), bond zone (BZ), heat affected zone (HAZ) and base material (BM). According to the hardness results, the symmetry axis of the welded joint sample was determined along with the lowest hardness point in the central area of the weld, and then the welded sample was cut out for the SCC test. The opening position of the sample and the direction of the prefabricated crack are shown in Figure 1.

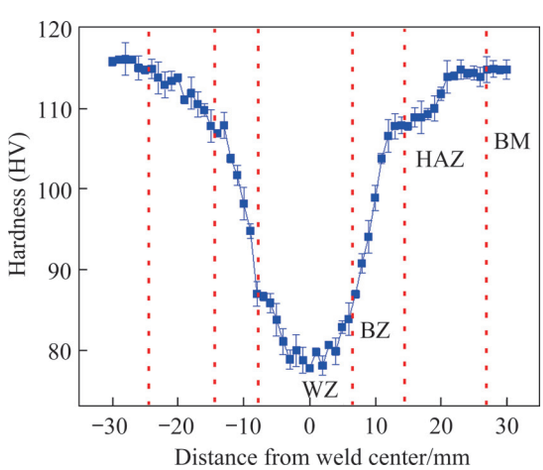


**Figure 2** Microhardness distribution curve of the alloy hot-rolled plate welded joint

### 2.4 Experimental procedure

According to GB 15970.6—2007 and GB/T 15970.9—2007 standards, the SCC susceptibility of BM and WZ in 3.5 wt.% NaCl solution was evaluated. All SCC tests were carried out on a Bairoe YYF-50 equipped with a DCPD crack propagation measurement system. Before testing, the samples were sonicated in acetone and deionized water for 10 min, respectively, and then dried with natural air. Here, the sample is a 0.5 T-CT sample with a width of $W$=25.4 mm and a thickness of $B$=12.7 mm. The specific size of the SCC sample is shown in Figure 3, and the sampling direction of the sample is shown in Figure 1. The prefabrication of fatigue cracks in CT samples refers to the GB/T 15970.9—2007 standard, and the prefabricated crack length is 2.0−2.5 mm.

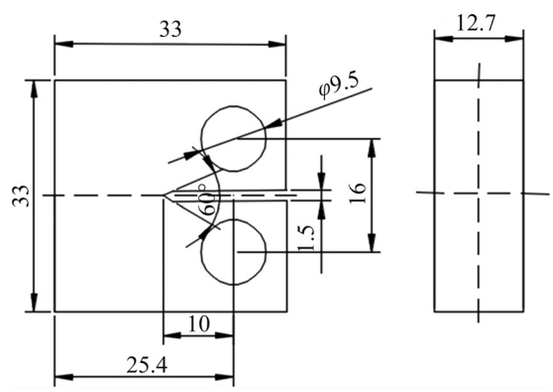


**Figure 3** Dimensions of SCC samples (unit: mm)

According to the GB/T 15970.9—2007 standard, the preloaded samples were exposed to NaCl solution for 24 h before the start of the SCC test. Then, SCC crack propagation tests were performed on BM and WZ at a displacement rate of $1\times10^{-6}$ mm/s.

The crack propagation was measured by the DCPD method, and the curve of crack propagation $a/W$ versus time $t$ was finally obtained. The DCPD method mainly used a constant current (2 A in this study) through the precracked sample and then

loaded the sample. As the crack propagated, the cross-sectional area of the unbroken sample decreased, increasing electrical resistance, and the potential difference across the crack increased with the length of crack propagation. Therefore, the potential signal could be converted into a real-time measurement of crack length ($a$) through the entire loading process. Figure 4 shows a schematic diagram of the potential measurement at the front and rear ends of the SCC sample. The measuring wires were made of 0.3 mm diameter copper wire, which was fixed to the sample surface by spot welding, and the welding points were sealed to prevent corrosion after welding. To ensure the repeatability of test results, each test was repeated three times. After the experiment, the SEM and EBSD samples were cut parallel to the side of the sample to observe the crack propagation path. The remainder of the sample continued to break on the MTS. Then, the surface morphology of the corrosion samples after fracture was observed using SEM.

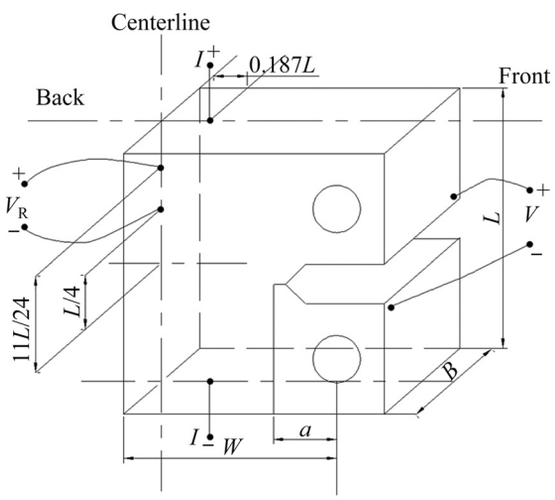


**Figure 4** Schematic diagram of potential measurement at the front and back ends of the SCC samples

The SCC samples of Al-Mg-Mn-Sc-Zr alloy BM and TIG welded joints were all machined from T-L oriented plates, the load was applied in the transverse (T) direction, and the crack propagated along the plane parallel to the longitudinal (L) direction. In this study, the SCC experimental method of CT pre-cracked samples was carried out on MTS loading equipment. The loading of the samples is shown in Figure 5.

When the samples were subjected to crack propagation tests in 3.5% NaCl solution, the feedback of crack propagation $a/W$ vs. time $t$ for BM and WZ was provided by the DCPD method (Figure 6). Then, the average crack propagation rate d$a$/d$t$ is obtained from the data in Figure 6.

**Figure 5** Sample loading diagram

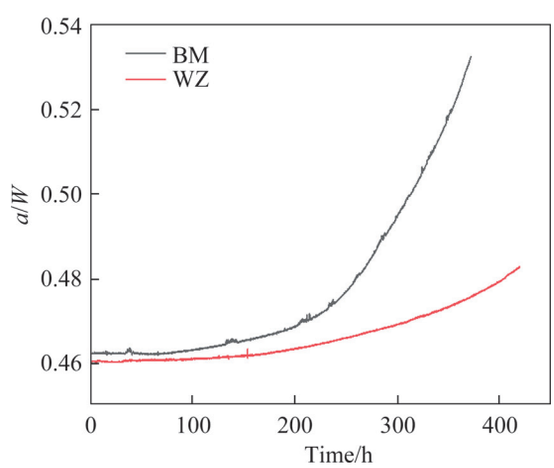


**Figure 6** The curve of $a/W-t$ of BM and WZ in 3.5% NaCl solution

## 3 Results and analysis

### 3.1 Microstructure analysis of TIG welded joints

To determine the effect of microstructure on SCC in different regions of Al-Mg-Mn-Sc-Zr alloy BM and TIG welded joints, SEM, EBSD, and TEM microstructures of different regions of BM and welded joints were investigated.

During the welding process, the welding heat input resulted in differences in the microstructure composition of the TIG welded joints. Figure 7 shows the microstructure and precipitated phase

sizes in different regions of the TIG welded joints of Al-Mg-Mn-Sc-Zr alloy. Fibrous grains were clearly visible in BM and a large number of precipitated phases of various sizes and morphologies were dispersed across the grain boundaries. The HAZ region had significantly coarser grains and fewer precipitation phases of different sizes and shapes compared to the BM region. Under the effect of welding thermal cycling, grain boundary segregation occurred in BZ. The grain morphology in WZ showed typical dendritic crystals, and the size of the precipitated phase in this region was small. The precipitated phases in different regions of the welded joints were investigated by EDS and the results are shown in Table 2. The main compositions of the white precipitated phases were Fe, Mg, Mn and Si elements. These intermetallic phases with different morphologies were confirmed to be Al (Mn, Fe) phases.

Figure 8 shows a general view of the EBSD

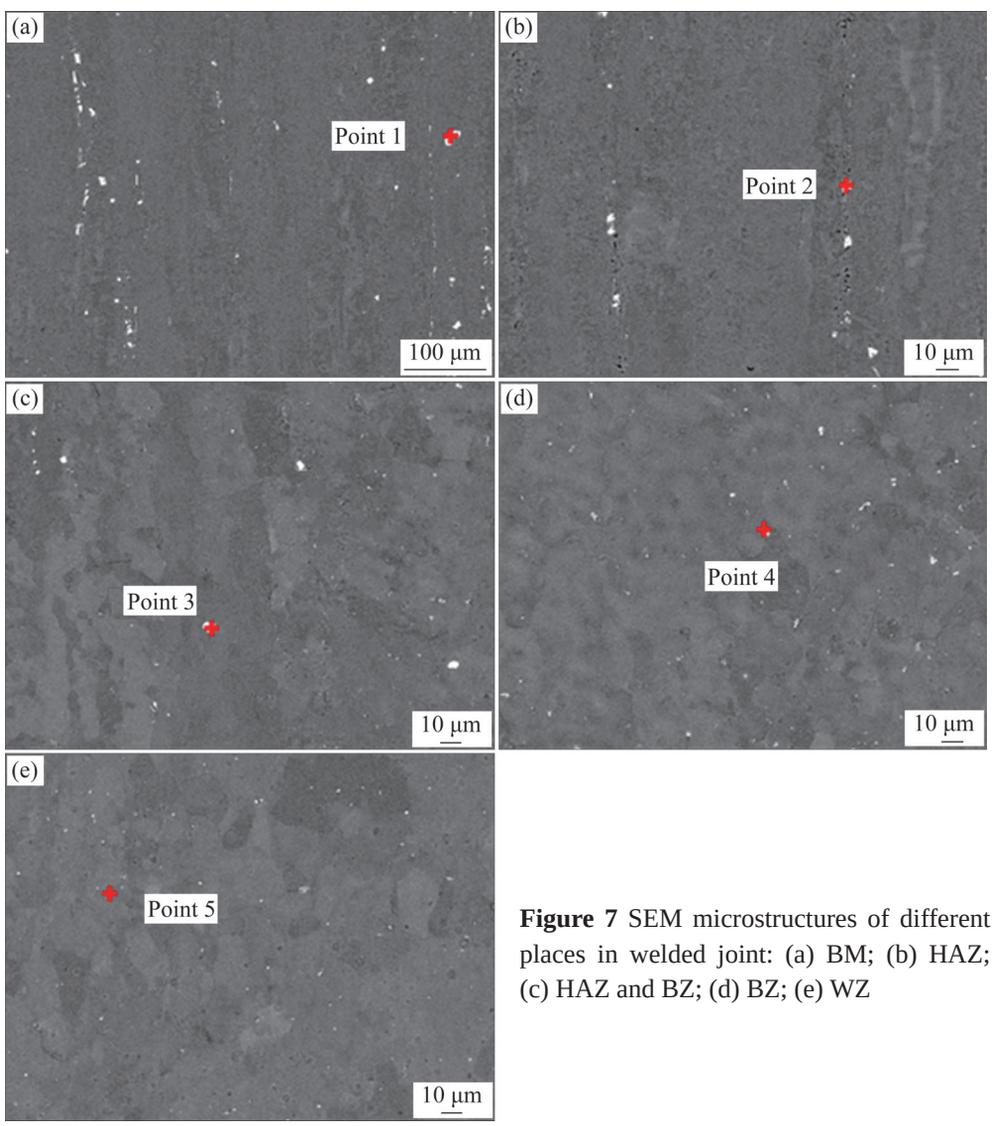


**Figure 7** SEM microstructures of different places in welded joint: (a) BM; (b) HAZ; (c) HAZ and BZ; (d) BZ; (e) WZ

**Table 2** EDS results of the precipitated phases in different areas of welded joints

| Weld area | Point | *w*(Al)/% | *w*(Mg)/% | *w*(Fe)/% | *w*(Mn)/% | *w*(Si)/% |
|---|---|---|---|---|---|---|
| BM | 1 | 86.09 | 5.89 | 5.49 | 2.12 | 0.41 |
| HAZ 1 | 2 | 89.59 | 6.41 | 1.60 | 2.05 | 0.35 |
| HAZ 2 | 3 | 85.02 | 5.11 | 5.84 | 3.79 | 0.24 |
| BZ | 4 | 84.25 | 6.98 | 6.01 | 2.53 | 0.23 |
| WZ | 5 | 83.24 | 5.73 | 8.43 | 2.39 | 0.21 |

analysis of the TIG welded joints of Al-Mg-Mn-Sc-Zr alloy. There was a significant recrystallisation behaviour in HAZ compared to BM. The grain morphology of BZ and WZ was equiaxed. The grain diameter in WZ was larger than that in BZ.

Figure 9 shows the EBSD maps of different regions of the TIG welded joints. Elongated grains along the rolling direction would be clearly visible in BM. HAZ was characterized by significant grain growth and recrystallisation compared to BM. BZ consisted of equiaxed grains with a grain size of about 10 μm. The diameter of the equiaxed grains in WZ varied from 20 μm to 80 μm.

Figure 10 shows the results of TEM microstructure analysis in the BM region of the TIG welded joints of Al-Mg-Mn-Sc-Zr alloy. It can be clearly seen that the organization of BM was dominated by restitution during the low-temperature stress relief annealing process. Lower dislocation densities were observed in BM and new grain nucleation was found in localized areas. There were spherical precipitates uniformly distributed within the grains of BM. Many studies have demonstrated that these spherical precipitates were co-lattice $Al_3$ (Sc, Zr) particles, which could effectively pin down dislocations and grain boundaries. Overall, the

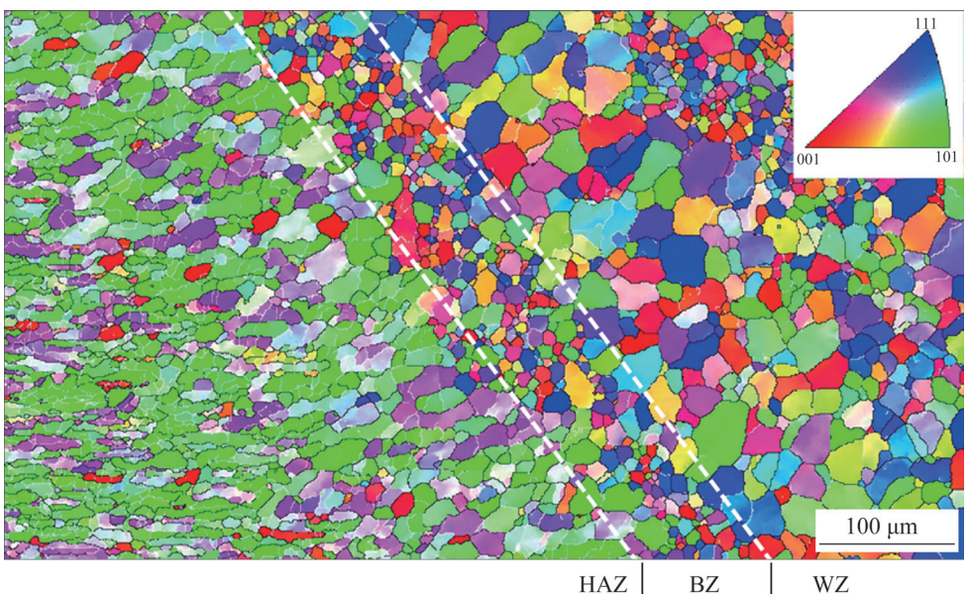


**Figure 8** EBSD diagram of TIG welded joint

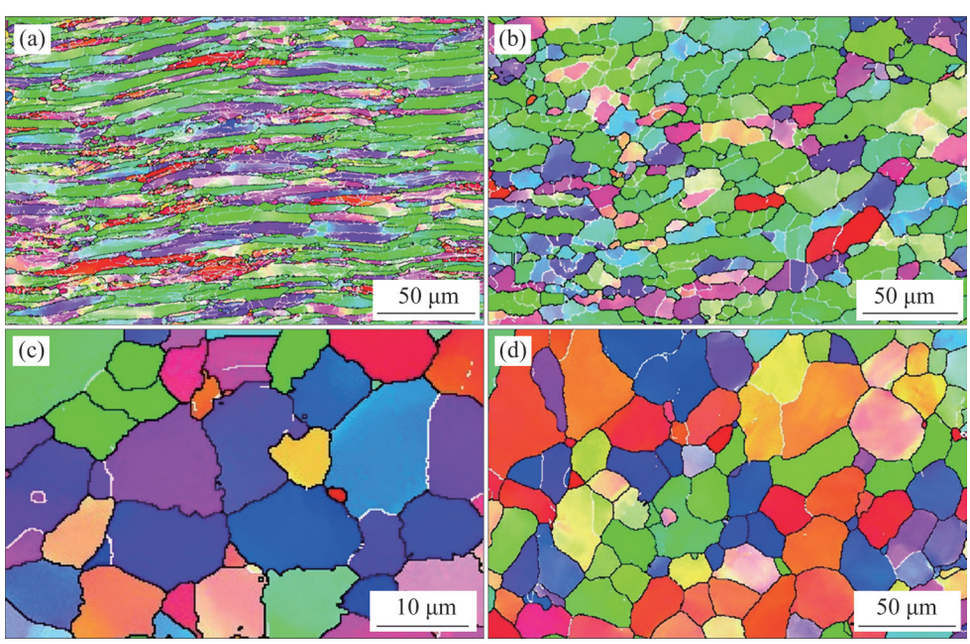


**Figure 9** EBSD maps of different regions of TIG welded joints: (a) BM; (b) HAZ; (c) BZ; (d) WZ

characteristics of the deformed tissue were still retained in BM, which not only ensured a certain alloy strength but also significantly released the deformation energy in the deformed tissue, thus reducing the possibility of thermal cracking during TIG welding.

During the welding process, the organization of the HAZ of the welded joint was affected by the welding heat as shown in Figures 11(a) and (b). The tissue in this region reverted, with more obvious recrystallisation and a polygonised structure, and the grains of the newly formed nuclei grew significantly. Notably, many dispersed $Al_3$(Sc, Zr) precipitation phase particles co-latticed with the

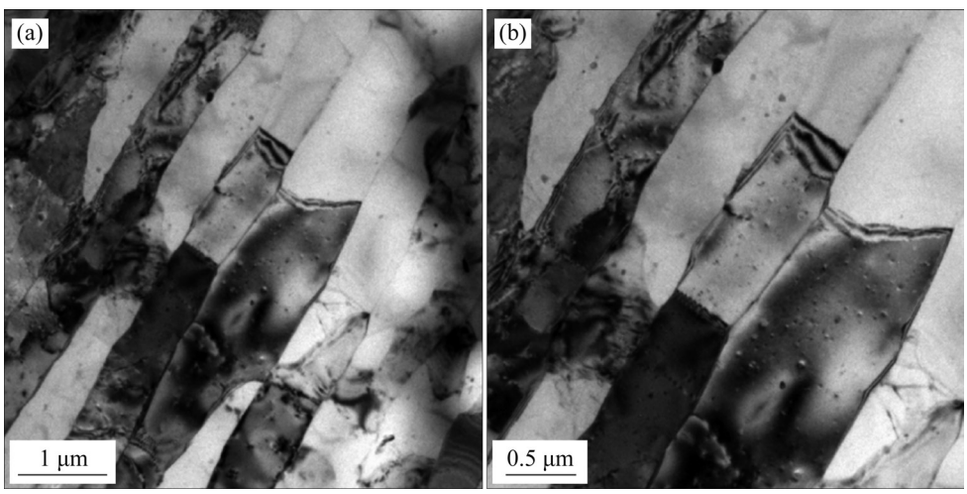


**Figure 10** TEM microstructure of BM

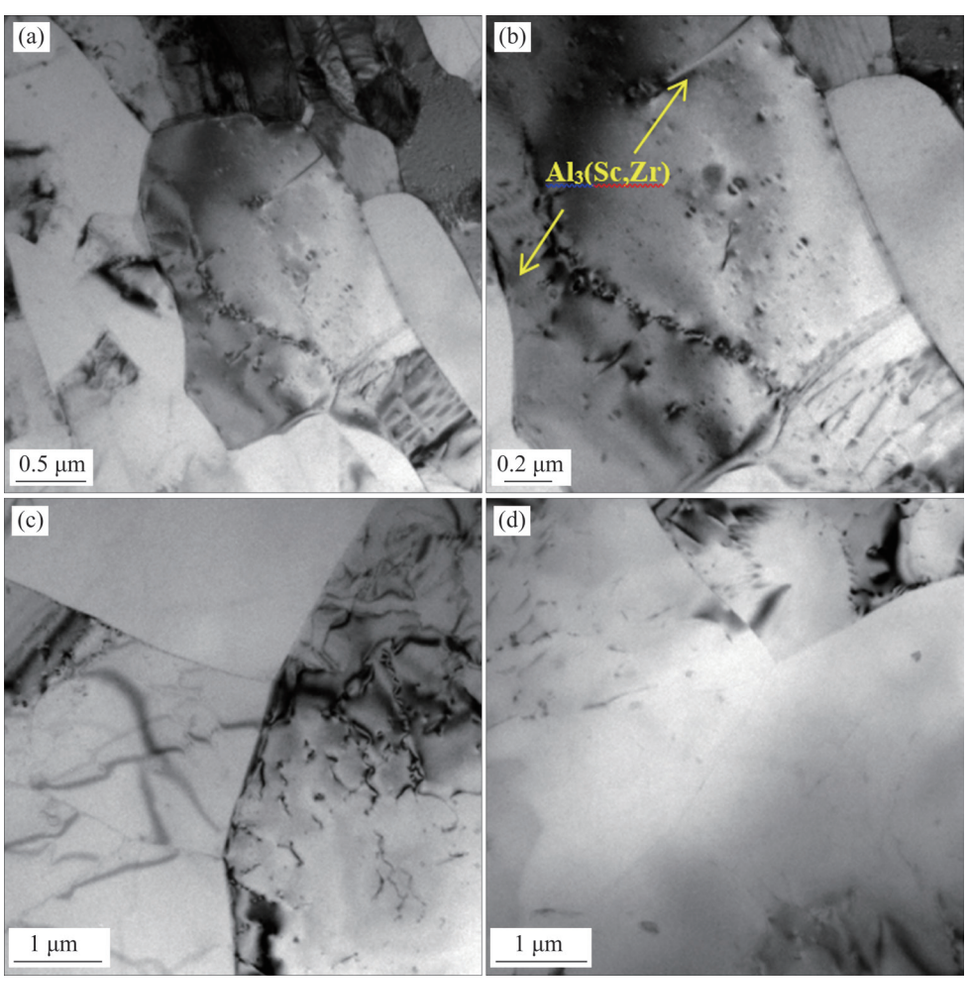


**Figure 11** TEM microstructures of different regions of welded joints: (a, b) HAZ; (c) BZ; (d) WZ

matrix were also observed in HAZ. Moreover, dislocations and subgrain boundaries can be seen pinned by $Al_3$(Sc, Zr) particles. Furthermore, the hardness of the $Al_3$(Sc, Zr) particles was high enough to strongly hinder the movement of dislocations during the welding process, thus inhibiting recrystallization. The interaction of these fine particles with dislocations and subgrain boundaries contributed to the suppression of grain coarsening. As shown in Figures 11(c) and (d), the BZ and WZ regions were very clean, and no precipitated phases were observed either within the grains or at the grain boundaries.

### 3.2 Macroscopic morphology of stress corrosion cracks

The macroscopic morphology of the BM and WZ samples after the SCC tests are shown in Figure 12. Apparently, after immersion in the corrosion liquid, there were no obvious corrosion marks on the surface of the sample, and only a small amount of corrosion products precipitated in the cracks of the sample.

Figure 13 shows the SEM morphology and EDS analysis results of the surface crack tip region of the sample after the SCC test. Obviously, the SCC cracks in both BM and WZ extended in the

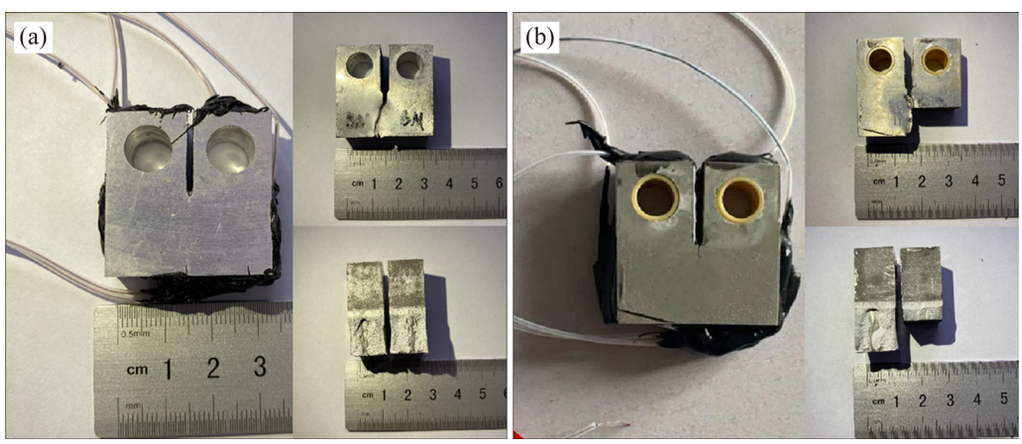


**Figure 12** Macromorphology of Al-Mg-Mn-Sc-Zr alloy sample after experiment: (a) BM; (b) WZ

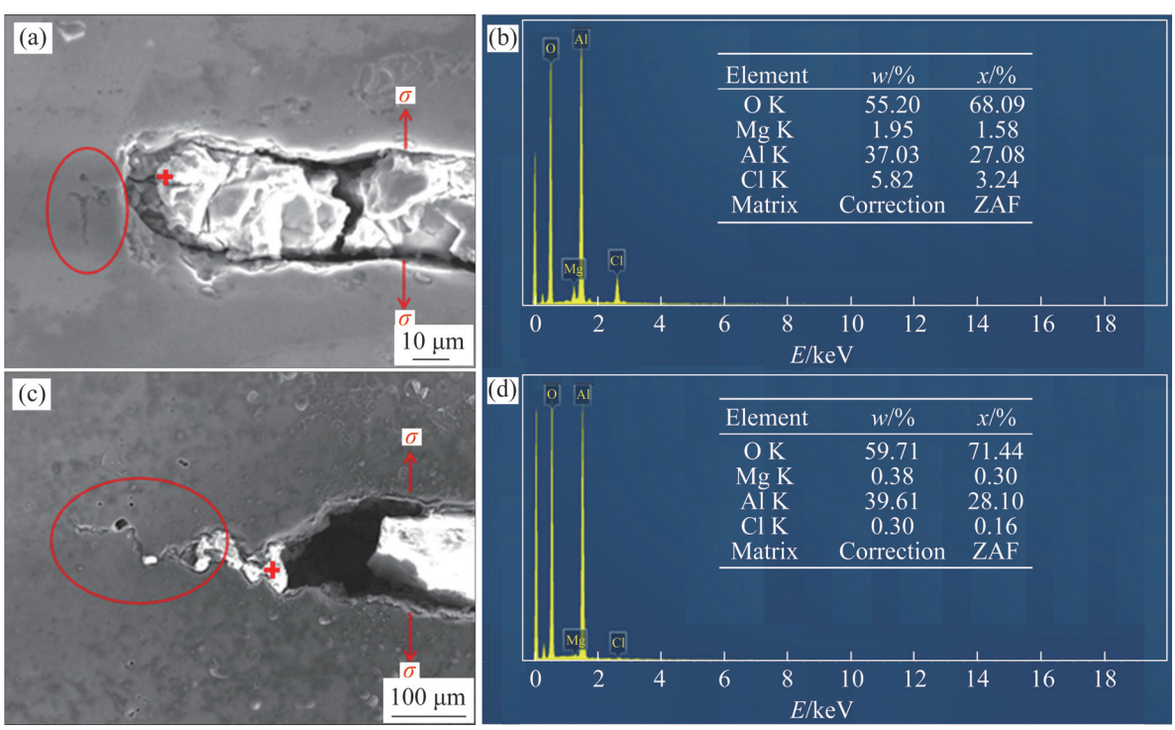


**Figure 13** Corrosion morphology and energy spectrum analysis at the crack tip of Al-Mg-Mn-Sc-Zr alloy: (a, b)BM; (c, d)WZ samples

direction perpendicular to the loading force. Moreover, severe corrosion occurred in the crack tip region, and numerous white corrosion products accumulated on the surface and cracks of the samples. EDS analysis of the corrosion products was performed to further analyze the elemental content of the corrosion products, and the results are shown in Figures 13(b) and (d). The results of the EDS analysis showed that the corrosion products in the crack tip region consisted mainly of Al and O, with a small amount of Cl. As shown in Figure 13(a), the SCC crack propagation of the BM was discontinuous and the cracks were slightly bifurcated, which showed obvious anodic dissolution characteristics. Besides, as shown in Figure 13(c), no obvious bifurcation was seen at the tip of the SCC crack in WZ, which exhibited hydrogen embrittlement characteristics.

### 3.3 SEM morphology of stress corrosion crack fracture surface

The microscopic morphology of the fracture surface after the SCC test of BM is shown in Figure 14. It can be clearly observed that the fracture surface (Figure 14(a)) was composed of two regions: the prefabricated crack region and the SCC region. The fracture morphology exhibited typical brittle fracture characteristics with uneven sections and no obvious traces of plastic deformation. Further, SCC cracks of different lengths growing along the rolling direction of the alloy were observed on the fracture.

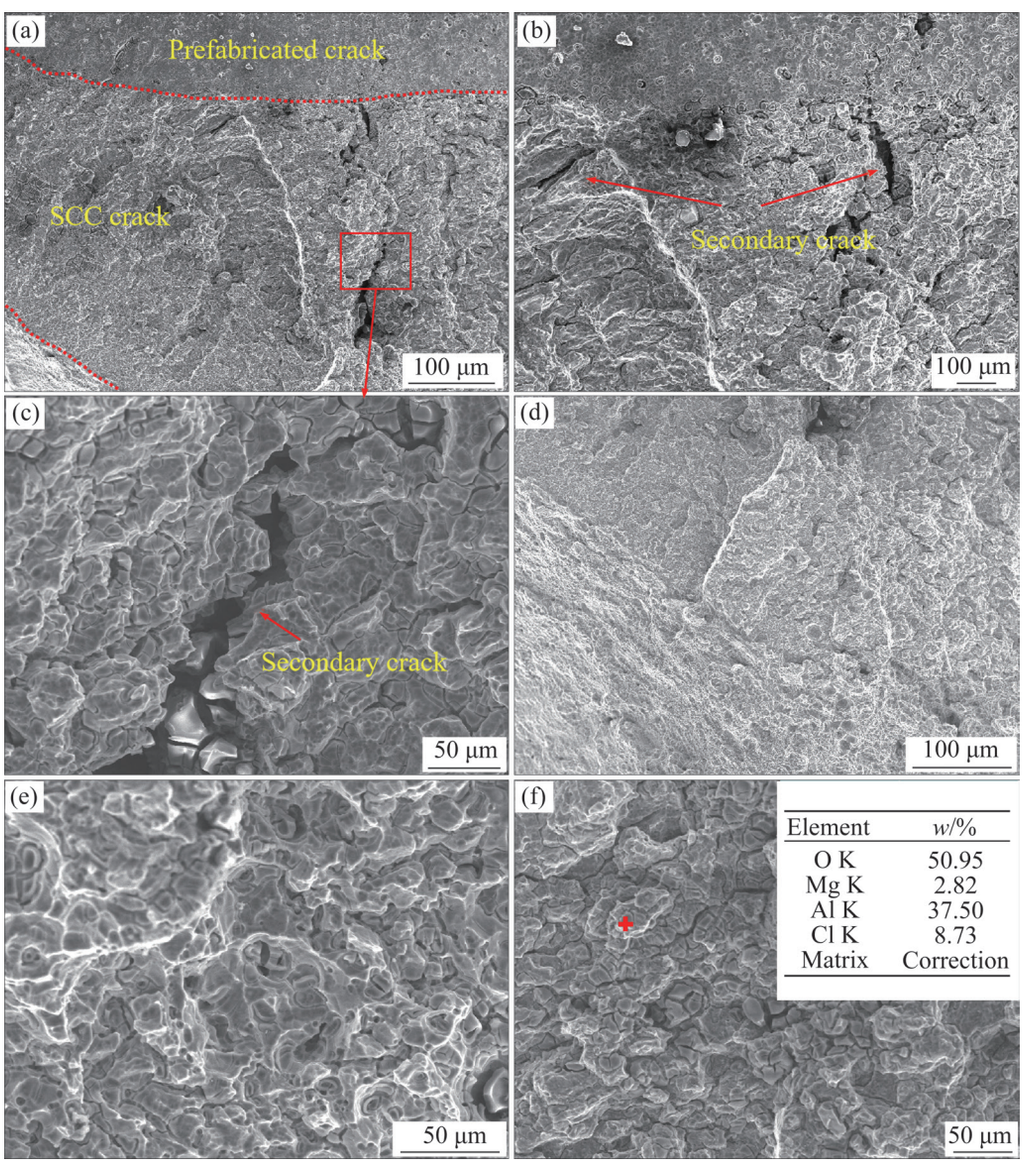


**Figure 14** SEM Morphology of fractures of BM samples: (a) Fracture morphology; (b) Inside the fracture; (c) Secondary crack; (d) Outside the fracture; (e) Dimples; (f) Corrosion products

As shown in Figures 14(b) and (c), secondary cracks appeared in the SCC zone and the direction of the cracks remained parallel to the rolling direction. In Figure 14(e), there were no significant corrosion products within the cracks, and the bottom of the cracks showed elongated secondary cracks. Numerous small and shallow dimples were distributed in the corrosion zone; however, no inclusions were found within the dimples. As shown in Figure 14(f), a significant amount of corrosion products deposited at the connection between the prefabricated cracked area and the stress corrosion zone. EDS detection was carried out to determine the composition of the corrosion products on the surface of the samples. The results showed that the corrosion products were mainly composed of Al, Mg, O and Cl.

Figure 15 illustrates the microscopic morphology of the fracture surface after the SCC test in the WZ region. The fracture crack direction showed obvious fracture characteristics along the grain, and obvious secondary cracks with large gaps distributed along the grain boundaries could be observed (Figures 15(c) and (d)). And, there were obvious traces of corrosion on the grain surface. Furthermore, it was possible to observe many large and deep dimples in the fracture (Figure 15(e)). The fracture showed cracking characteristics due to prolonged immersion of the fracture in the corrosive solution (Figure 15(d)). The results of EDS analysis showed that the corrosion products at the fracture mainly contained Al, O, Cl, Mg and other elements.

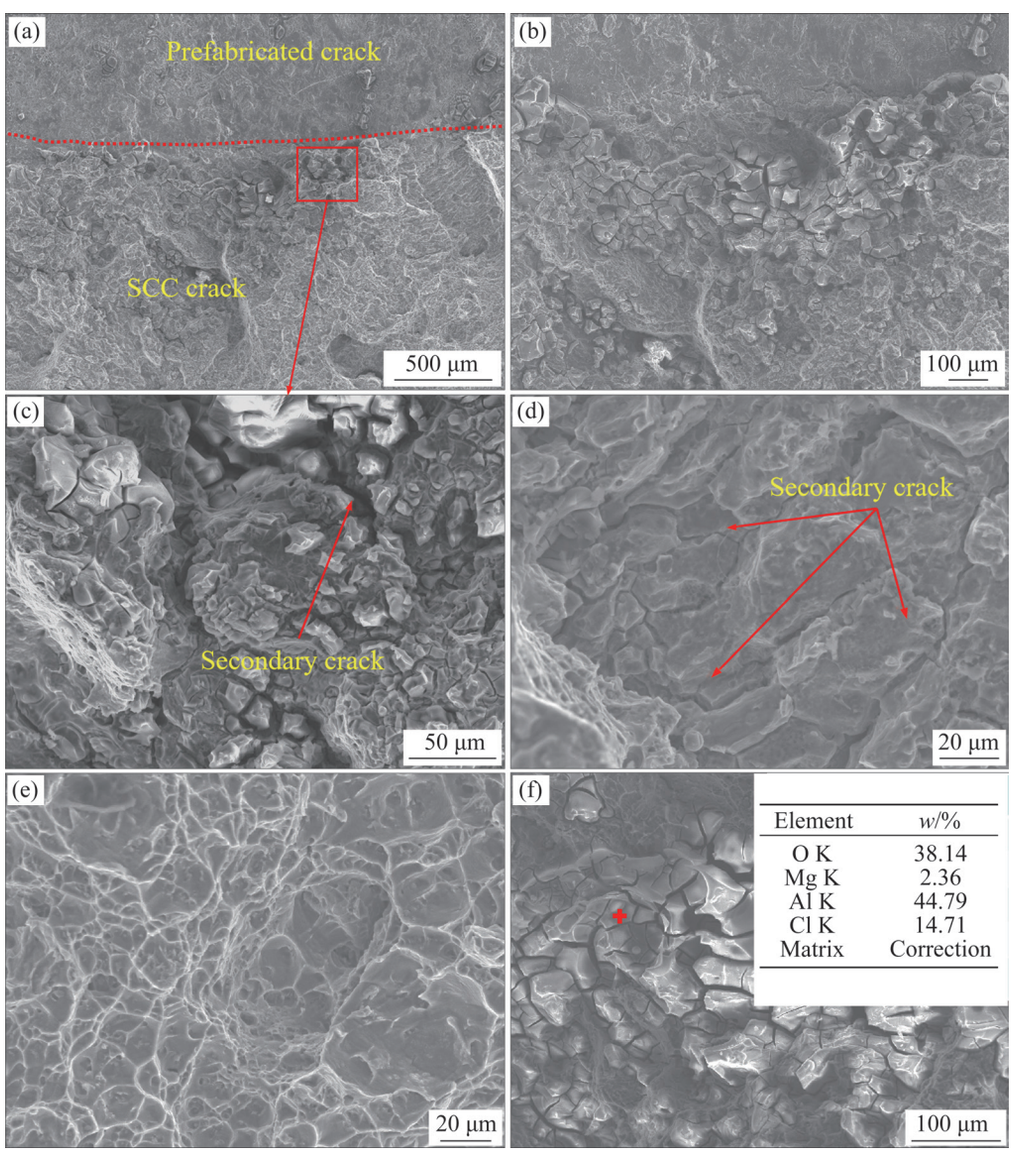


**Figure 15** SEM morphology of fractures of WZ samples: (a) Fracture morphology; (b) Fracture interior; (c) Secondary cracks; (d) Secondary cracks; (e) Dimples; (f) Corrosion products

The EDS results demonstrated that the corrosion products in this test were predominantly aluminates.

### 3.4 EBSD morphology of stress corrosion cracks

To further characterize the SCC crack propagation in the BM and WZ region, the propagation path at the crack tip was characterized by EBSD, as shown in Figure 16.

As can be seen in the figure, the grains of the BM exhibited typical rolling characteristics. The observation that SCC occurred inside the grains could be because the tip region of the prefabricated cracks just rested inside the grains. The propagation path of the stress corrosion crack was discontinuous, and there was obvious bifurcation at the tip of the main crack (Figure 16(a)). The fracture mode of Al-Mg-Mn-Sc-Zr alloy in the test was transgranular fracture. The grains in the center region of the WZ (Figure 16(c)) were equiaxed grains. The crack propagation in the WZ mainly proceeded along the grain boundaries while exhibiting discontinuities, and no bifurcation was shown at the crack tip. However, the transgranular fracture was exhibited in the red-marked region.

Additionally, the KAM plots of the BM and WZ (Figures 16(b) and (d)) showed higher values of localized orientation differences on both sides of the cracks and grain boundaries. This indicated that there was a large plastic deformation or a high defect density in this region.

### 3.5 Results for SCC crack propagation

Figure 17 shows plots of data for d$a$/d$t$ and $K_J$ (actual loaded stress intensity factor) versus time for the BM and WZ. The crack propagation rate was calculated according to the incremental polynomial method of crack propagation rate in GB/T 15970.2. According to the provisions in GB/T 15970.9—2007 standard, $K_J$ was calculated as follows:

$$K_J = \frac{YP}{B\sqrt{W}} \tag{1}$$

in the formula:

$$Y = \frac{2+\frac{a}{W}}{\sqrt{\left(1-\frac{a}{W}\right)^3}}\left[0.886+4.64\left(\frac{a}{W}\right)-13.32\left(\frac{a}{W}\right)^2+14.72\left(\frac{a}{W}\right)^3-5.6\left(\frac{a}{W}\right)^4\right] \tag{2}$$

In Eq. (2), $K_J$ was the actual loading stress intensity factor of the sample; $Y$ was the stress intensity factor coefficient; $P$ was the actual load applied to the sample; $B$ was the thickness of the

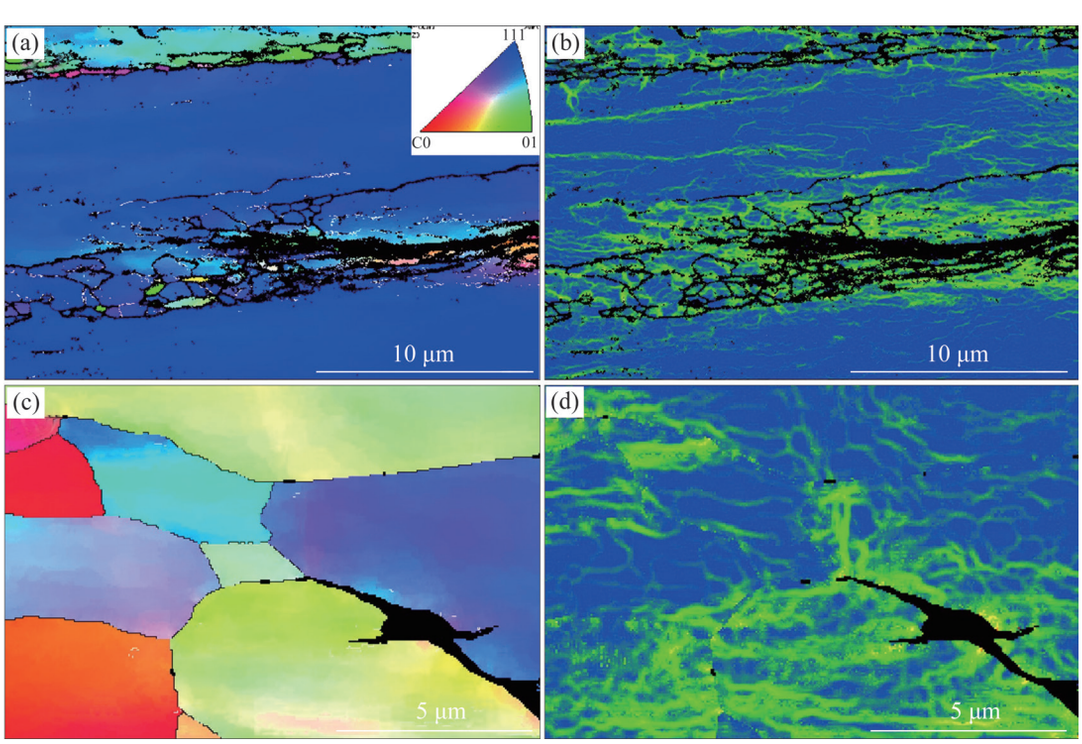


**Figure 16** EBSD morphology (a, c) and KAM (b, d) image of SCC crack propagation path of Al-Mg-Mn-Sc-Zr alloy samples: (a, b) BM; (c, d) WZ

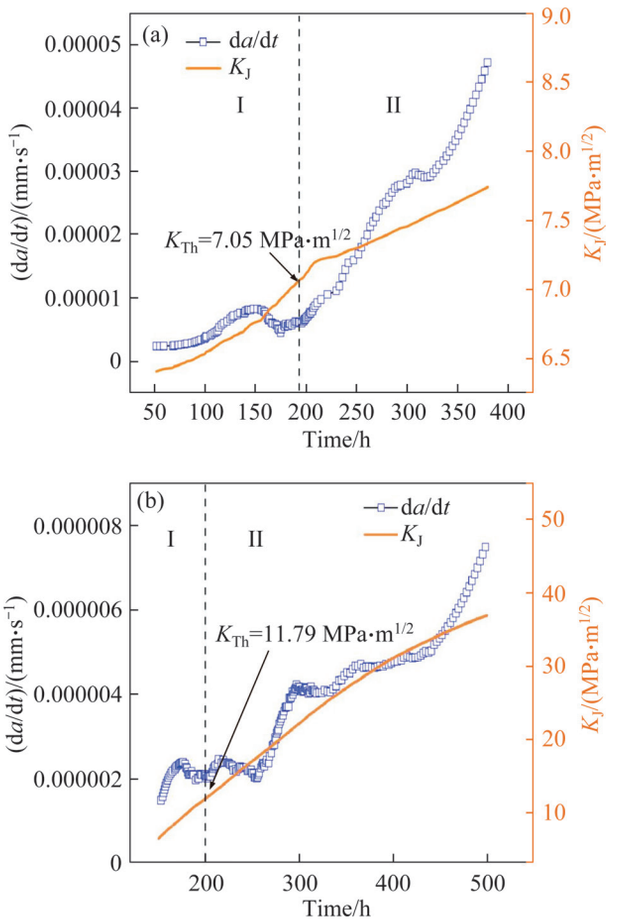


**Figure 17** d$a$/d$t$ and $K_J$ vs. time for BM (a) and WZ (b) immersed in 3.5% NaCl solution

sample; $W$ was the width of the sample, and $a$ was the effective crack length for crack propagation.

The various stages of SCC crack propagation can be determined from the data in Figure 17, and the relevant parameters are derived as clearly shown in Table 3. The increase in d$a$/d$t$ in stage I did not represent true crack propagation, but rather indicated the effect of crack tip plasticity on resistivity. This behavior would lead to an increase in errors in the measured potential, which the DCPD method converted into an indication of crack propagation. At this stage, the stress intensity factor $K_J$ produced at the crack tip by the applied load increased slowly with time but was not sufficient for the sample to undergo SCC. When the stress intensity factor exceeded $K_{Th}$, stage II was entered and SCC began to propagate. Thus, $K_{Th}$ was defined as the onset of SCC-dominated fracture and was shown in the figure as the onset of a significant increase in the slope of d$a$/d$t$ versus $K_J$ [27]. At this point, the value of the stress intensity factor $K_{Th}$ was equivalent to the value of $K_{ISCC}$, and d$a$/d$t$ was defined as the crack propagation rate. The d$a$/d$t$ increased rapidly with increasing $K_J$.

**Table 3** Parameters related to SCC crack propagation of BM and WZ

| Sample | Initial crack length, $a_0$/mm | $K_{Th}/K_{ISCC}$ |
|---|---|---|
| BM | 9.96 | 7.05 |
| WZ | 9.99 | 11.79 |

From the figure, the average crack propagation rate of SCC increased with the increase of the stress intensity factor. Under the same loading conditions, the average crack propagation rate of the BM was faster than that of the WZ. Figure 17 indicates the difference in SCC susceptibility between the BM and the WZ. Compared with the WZ, the BM has a lower $K_{Th}$ value and a higher d$a$/d$t$ rate, exhibiting higher SCC susceptibility. Moreover, the $K_{ISCC}$ of the BM was about 7.05 MPa·m$^{1/2}$, and the $K_{ISCC}$ of the WZ was about 11.79 MPa·m$^{1/2}$. However, the WZ required a higher stress intensity to initiate the SCC, so greater loads were realized during the test.

To further verify the difference in corrosion susceptibility between BM and WZ, a nitric acid weight loss experiment was carried out to determine the intergranular corrosion (IGC) performance of BM and WZ. The mass loss per unit area is shown in Figure 18. The mass losses were 83.2 and 33.8 mg/cm$^2$ for BM and WZ, respectively. According to the standard ASTM B928/B928M-09, both the BM and WZ were in the intergranular corrosion sensitive area, and the mass loss of BM was much greater than that of WZ, which indicated

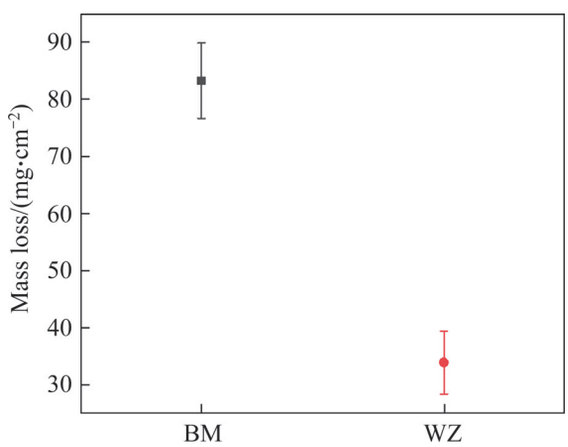


**Figure 18** Nitric acid mass loss values for BM and WZ

that BM had a higher sensitivity to intergranular corrosion. This corresponded to the higher SCC sensitivity of BM.

## 4 Discussion

### 4.1 SCC mechanisms

It was well known that anodic dissolution of $\beta$ phase precipitates at grain boundaries was the most commonly accepted theory for SCC of Al-Mg alloys [28 − 31]. However, a combination of OM, SEM, EBSD, and TEM microstructures of BM and TIG welded joints of Al-Mg-Mn-Sc-Zr alloys indicated that no significant $\beta$ phase precipitates were observed at grain/sub-grain boundaries in this study. Furthermore, some researchers argued that hydrogen embrittlement also plays a role in causing and exacerbating SCC [32]. When stress was applied to the samples, severe stress concentrations were generated in the crack tip region of the samples, resulting in lattice defects (vacancies, dislocations) and precipitates accumulating there. This environment provided more trapping sites for hydrogen diffusion, leading to hydrogen bubble nucleation. Consequently, the electrochemical activity in this region was enhanced. It has been shown that the crack tip region of high-strength aluminum alloys has a more negative corrosion potential compared to the matrix [33]. According to corrosion electrochemistry, when the samples were subjected to SCC tests in 3.5% NaCl solution, anodic dissolution first occurred in the crack tip region of the BM and WZ, and critical defects were formed. The relevant anodic reaction equation was given below:

$$\mathrm{Al(matrix)} \rightarrow \mathrm{Al^{3+}} + 3\mathrm{e^-} \tag{3}$$

The following reactions occurred at the cathode:

$$\mathrm{O_2} + 2\mathrm{H_2O} + 4\mathrm{e^-} \rightarrow 4\mathrm{OH^-} \tag{4}$$

$$2\mathrm{H^+} + 2\mathrm{e^-} \rightarrow \mathrm{H_2(g)} \tag{5}$$

Simultaneously, the gap at the crack tip was blocked by a large amount of corrosion products, creating a closed environment. The $Al^{3+}$ generated in the solution would undergo the following hydrolysis reactions and a complex series of hydroxyl chloride precipitates would also occur [34], which would further acidify the crack tip region:

$$\mathrm{Al^{3+}} + 3\mathrm{H_2O} \rightarrow \mathrm{Al(OH)_3} + 3\mathrm{H^+} \tag{6}$$

$$2\mathrm{Al} + 3\mathrm{H_2O} \rightarrow \mathrm{Al_2O_3} + 6\mathrm{H^+} + 6\mathrm{e^-} \tag{7}$$

$$\mathrm{Al^{3+}} + \mathrm{Cl^-} \rightarrow \mathrm{AlCl^{2+}} \tag{8}$$

$$\mathrm{AlCl^{2+}} + 2\mathrm{H_2O} \rightarrow \mathrm{Al(OH)_2Cl} + 2\mathrm{H^+} \tag{9}$$

According to Eq. (7), a passivation film of $Al_2O_3$ would be formed on the surface of the newly exposed alloy. However, the narrow crack tip had a limiting effect on the expansion of the solution inside the crack. Hence, a large amount of $Al^{3+}$ from anodic dissolution and a large amount of $H^+$ from hydrolysis accumulated in the crack and could not expand outwards. To maintain the charge balance of the solution in the crack, the reactive ion $Cl^-$ in the solution migrated toward the crack tip, where it adsorbed and accumulated. $Cl^-$ had a strong destructive effect on the oxide film on the surface of aluminum alloys, which resulted in direct contact between the newly exposed aluminum alloy surface and the 3.5% NaCl solution. Thus, the dissolution at the crack tip of the aluminum alloy was accelerated, resulting in a continuous forward propagation of the corrosion crack. Hydrolysis of $Al^{3+}$ at the crack tip in NaCl solution generated a large amount of $H^+$, which further acidified the crack tip and led to a decrease in pH in the region, thus accelerating the dissolution of the alloy. It also provided the necessary conditions for the precipitation of hydrogen and the movement of hydrogen into the interior of the material. The above process alternated repeatedly, which resulted in a continuous forward propagation of the corrosion cracks at the tip.

### 4.2 Effect of microstructure on crack propagation

There was a stress gradient between the crack tip region and the matrix of the aluminum alloy, which was capable of inducing hydrogen diffusion. Therefore, hydrogen would diffuse under stress to the crack tip region where the stress was concentrated. Additionally, hydrogen moved with dislocations [35]. Moreover, hydrogen had a pinning effect on dislocations [36]. As d$a$/d$t$ increased, a large amount of hydrogen migrated with the dislocations to the crack tip due to the larger

increment of crack advancement, leading to the formation of a high density of dislocations in the tip region (Figure 16(a)). Hence, hydrogen atoms generated by the cathodic reaction entered the plastic zone at the crack tip through dislocations. Hydrogen aggregation and adsorption at the crack tip could weaken the interatomic bonding force, which would lead to the embrittlement of the alloy. Moreover, hydrogen atoms combined to form $H_2$ molecules when their concentration reached a critical value. The rapid expansion of the $H_2$ molecules generated a huge internal pressure inside the aluminum alloy, which led to the creation of internal cracks. Thus, the diffusion and aggregation of hydrogen promoted transgranular cracking. This would correspond to the discontinuity in SCC crack propagation in Figure 16. Combined with Figure 17(a), the crack propagation of the BM was affected by the diffusion of H at the crack tip, which resulted in a steady upward trend in the SCC crack propagation rate until $K_J$ approached and exceeded the critical stress intensity for fracture.

Generally, grain boundaries were strong trap sites for hydrogen. The formation of hydrogen traps reduced the mobility of hydrogen. Hydrogen atoms continued to aggregate and formed hydrogen molecules, thus generating hydrogen pressure. Consequently, this led to cracks along grain boundaries, and the cracks at the grain boundaries were not connected to the main crack. Furthermore, the presence of Al(Mn, Fe) particles on the grain boundaries led to anodic dissolution of the Al matrix and oxide layer around the particles, which would cause concave pits. Additionally, the study demonstrated that $Al_3$(Sc, Zr) particles are only slightly cathodic to the surrounding Al matrix, which was insufficient to promote microelectrochemical corrosion at the interface of the particles with aluminum. Therefore, Al(Mn, Fe) particles dominated in our studied alloys compared to $Al_3$(Sc, Zr) particles. Meanwhile, the pits would accelerate to expand under externally applied stresses, which would cause the cracks to grow toward the inside of the grains, as shown by the red ellipse mark in Figure 16(c). Therefore, the fracture mode of SCC exhibited a mixed fracture mechanism of transgranular and intergranular. Combined with the crack propagation rate of the WZ in Figure 17(b), it could be seen that in the early stage of crack propagation, the crack propagation rate was fast due to the cathodic and hydrolysis reactions, and the crack propagation rate became slow in the later stage can be attributed to the limitation of hydrogen mobility by the strong hydrogen trap. Brittle intergranular damage at the fracture in BM and WZ of TIG welded Al-Mg-Mn-Sc-Zr alloys indicated SCC related to hydrogen embrittlement.

Combined with SEM, EBSD and TEM analyses, it can be concluded that the BM of TIG welded Al-Mg-Mn-Sc-Zr alloy mainly formed relatively continuous anodic dissolution channels inside the grains in the SCC crack propagation tests, which resulted in transgranular fracture, and the main cracks propagated along the direction of rolling, and the fracture schematic diagram is shown in Figure 19(a). The central region of the WZ underwent recrystallization behavior due to the high welding heat, resulting in the formation of relatively defect-free equiaxed grains, which led to the propagation of SCC cracks in WZ mainly along the curved grain boundaries. The presence of

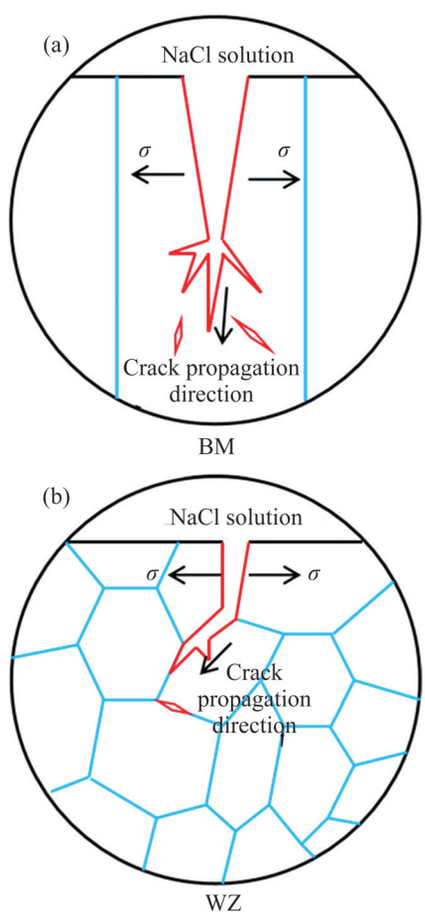


**Figure 19** Schematic diagram of the stress corrosion fracture model of the BM (a) and WZ (b)

precipitates at grain boundaries could initiate pitting, resulting in crack propagation into the interior of the grain. Thus, a mixed fracture mechanism of intergranular and transgranular fracture was generated. The fracture schematic diagram is shown in Figure 19(b).

## 5 Conclusions

In this paper, the SCC crack propagation behaviour of BM and WZ of TIG welded Al-Mg-Mn-Sc-Zr alloy was investigated by the DCPD method, and the curves of crack propagation of BM and WZ as a function of time were obtained, and the mechanism of crack propagation was revealed. The following conclusions were drawn:

1) There was a significant difference in the stress corrosion susceptibility of BM and WZ of TIG welded Al-Mg-Mn-Sc-Zr alloys. The SCC crack propagation rate in BM was faster than in WZ, and the WZ exhibited a lower susceptibility to SCC. Also, the $K_{ISCC}$ in BM of TIG welded Al-Mg-Mn-Sc-Zr alloy was 7.05 MPa·m$^{1/2}$, and that in WZ was 11.79 MPa·m$^{1/2}$.

2) The SCC crack of the BM and WZ of TIG welded Al-Mg-Mn-Sc-Zr alloy showed brittle fracture characteristics. The crack propagation was attributed to the combined effect of anodic dissolution and hydrogen embrittlement. Enriching hydrogen atoms at hydrogen trap locations led to hydrogen embrittlement, which initiated the growth of discontinuous cracks.

3) The SCC crack propagation rate of BM and WZ of TIG-welded Al-Mg-Mn-Sc-Zr alloys was affected by the dislocations at the crack tip. Particularly, many dislocations near the grain boundary of the BM enhanced the hydrogen diffusion rate, leading to faster SCC crack propagation in BM than in WZ.

## Contributors

The overarching research goals were developed by TANG Zhong-qin and JIANG Feng. TANG Zhong-qin analyzed the measurement data and wrote the first draft of the manuscript. JIANG Feng verified the results and edited the manuscript. LONG Meng-jun, YE Peng-cheng, and WU Ming-jin provided technical support. All authors replied to the reviewers' comments and revised the final version.

## Conflict of interest

TANG Zhong-qin, JIANG Feng, LONG Meng-jun, YE Peng-cheng, and WU Ming-jin declare that they have no conflict of interest.

## References

[1] XUE D, WEI W, SHI W, et al. Optimization of stabilized annealing of Al-Mg alloys utilizing machine learning algorithms [J]. Materials Today Communications, 2023, 35: 106177. DOI: 10.1016/j.mtcomm.2023.106177.

[2] FILATOV Y A, YELAGIN V I, ZAKHAROV V V. New Al-Mg-Sc alloys [J]. Materials Science and Engineering A, 2000, 280(1): 97 − 101. DOI: 10.1016/S0921-5093(99)00673-5.

[3] HUANG Yu-shen, SUN Peng, SUN Lin-lin, et al. Effect of Zn/Mg ratio on aging precipitates and mechanical property of high Mg content Al-Mg-Zn alloys with Sc and Zr additions [J]. Journal of Alloys and Compounds, 2024, 976: 173368. DOI: 10.1016/j.jallcom.2023.173368.

[4] XU Pian, JIANG Feng, JIANG Jing-yu, et al. Morphology evolution and growth mechanism of primary $Al_3Sc$ and eutectic $Al_3Sc$ in Al-Sc alloys [J]. Journal of Materials Research and Technology, 2023, 26: 5910 − 5920. DOI: 10.1016/j.jmrt.2023.08.280.

[5] HUANG Hong-feng, JIANG Feng, ZHOU Jiang, et al. Hot deformation behavior and microstructural evolution of as-homogenized Al-6Mg-0.4Mn-0.25Sc-0.1Zr alloy during compression at elevated temperature [J]. Journal of Alloys and Compounds, 2015, 644: 862 − 872. DOI: 10.1016/j.jallcom.2015.05.048.

[6] LI Meng-jia, LIAN Juan, CAO Ling-fei, et al. Effect of platform temperature on microstructure and corrosion resistance of selective laser melted Al-Mg-Sc alloy plate [J]. Journal of Central South University, 2022, 29(3): 999−1014. DOI: 10.1007/s11771-022-4959-z.

[7] SHEN Jiao-jiao, CHEN Biao, WAN Jie, et al. Effect of annealing on microstructure and mechanical properties of an Al-Mg-Sc-Zr alloy [J]. Materials Science and Engineering A, 2022, 838: 142821. DOI: 10.1016/j.msea.2022.142821.

[8] QIU You-cai, YANG Xiao-fang, LI Jing-xiao, et al. The influence of Sc and Zr additions on microstructure and corrosion behavior of AA5182 alloy sheet [J]. Corrosion Science, 2022, 199: 110181. DOI: 10.1016/j. corsci. 2022. 110181.

[9] XIA Yun-hao, CAI Xiao-yu, DONG Bo-lun, et al. Wire arc additive manufacturing of Al-Mg-Sc alloy: An analysis of the effect of Sc on microstructure and mechanical properties [J]. Materials Characterization, 2023, 203: 113116. DOI: 10.1016/j.matchar.2023.113116.

[10] JIANG Jing-yu, JIANG Feng, ZHANG Meng-han, et al. Study on impact toughness and fracture behaviour of an Al-Mg-Sc alloy [J]. Vacuum, 2023, 211: 111926. DOI: 10.1016/j.vacuum.2023.111926.

[11] AYDıN H, BAYRAM A, UĞUZ A, et al. Tensile properties of friction stir welded joints of 2024 aluminum alloys in different heat-treated-state [J]. Materials & Design, 2009, 30(6): 2211−2221. DOI: 10.1016/j.matdes.2008.08.034.

[12] VYSOTSKII I, MALOPHEYEV S, MIRONOV S, et al. Deformation behavior of friction-stir welded Al-Mg-Mn alloy with ultrafine-grained structure [J]. Materials Characterization, 2022, 185: 111758. DOI: 10.1016/j.matchar.2022.111758.

[13] CHEN Wei, WANG Wen-xian, LIU Ze-peng, et al. Improvement in tensile strength of Mg/Al alloy dissimilar friction stir welding joints by reducing intermetallic compounds [J]. Journal of Alloys and Compounds, 2021, 861: 157942. DOI: 10.1016/j.jallcom.2020.157942.

[14] MURALIDHARAN S, DINAKAR N. A comparative investigation on weld metal properties of similar and dissimilar TIG welded joints on Al-Mg alloys [J]. Materials Today: Proceedings, 2022, 62: 2217−2223. DOI: 10.1016/j.matpr.2022.03.373.

[15] LALVANI H, MANDAL P. Cold forming of Al-5251 and Al-6082 tailored welded blanks manufactured by laser and electron beam welding [J]. Journal of Manufacturing Processes, 2021, 68: 1615 − 1636. DOI: 10.1016/j. jmapro.2021.06.070.

[16] LEI Xue-feng, DENG Ying, YIN Zhi-min, et al. Tungsten inert gas and friction stir welding characteristics of 4-mm-thick 2219-T87 plates at room temperature and −196 ℃ [J]. Journal of Materials Engineering and Performance, 2014, 23(6): 2149−2158. DOI: 10.1007/s11665-014-1013-9.

[17] LIYAKAT N A, VEEMAN D. Improvement of mechanical and microstructural properties of AA 5052-H32 TIG weldment using friction stir processing approach [J]. Journal of Materials Research and Technology, 2022, 19: 332 − 344. DOI: 10.1016/j.jmrt.2022.05.015.

[18] MUÑOZ A C, RÜCKERT G, HUNEAU B, et al. Comparison of TIG welded and friction stir welded Al-4.5Mg-0.26Sc alloy [J]. Journal of Materials Processing Technology, 2008, 197(1 − 3): 337 − 343. DOI: 10.1016/j.jmatprotec.2007.06.035.

[19] YANG Dong-xia, LI Xiao-yan, HE Ding-yong, et al. Study on microstructure and mechanical properties of Al-Mg-Mn-Er alloy joints welded by TIG and laser beam [J]. Materials & Design, 2012, 40: 117−123. DOI: 10.1016/j.matdes.2012.03.041.

[20] SU Dan, ZHANG Jia-yi, WANG Bin. The microstructure and weldability in welded joints for AA 5356 aluminum alloy after adding modified trace amounts of Sc and Zr [J]. Journal of Manufacturing Processes, 2020, 57: 488 − 498. DOI: 10.1016/j.jmapro.2020.07.017.

[21] MENZEMER C, LAM P C, SRIVATSAN T S, et al. An investigation of fusion zone microstructures of welded aluminum alloy joints [J]. Materials Letters, 1999, 41(4): 192−197. DOI: 10.1016/S0167-577X(99)00129-9.

[22] YANG Dong-xia, LI Xiao-yan, NIE Zuo-ren, et al. Microstructure characteristics of TIG welded Al-Mg alloy with small amount Er addition [J]. Rare Metal Materials and Engineering, 2012, 41(10): 1713−1716.

[23] SUBBAIAH K. Microstructure and mechanical properties of tungsten inert gas welded joints of cast Al-Mg-Sc alloy [J]. Materials Today: Proceedings, 2019, 16: 248 − 253. DOI: 10.1016/j.matpr.2019.05.086.

[24] BABU N K, BHIKANRAO P Y, SIVAPRASAD K. Enhanced mechanical properties of AA5083 GTA weldments with current pulsing and addition of scandium [J]. Materials Science Forum, 2013, 765: 716 − 720. DOI: 10.4028/www.scientific.net/msf.765.716.

[25] XU Guo-fu, QIAN Jian, XIAO Dan, et al. Mechanical properties and microstructure of TIG and FSW joints of a new Al-Mg-Mn-Sc-Zr alloy [J]. Journal of Materials Engineering and Performance, 2016, 25(4): 1249 − 1256. DOI: 10.1007/s11665-016-1942-6.

[26] ANDRESEN P L, MORRA M M. IGSCC of non-sensitized stainless steels in high temperature water [J]. Journal of Nuclear Materials, 2008, 383(1, 2): 97−111. DOI: 10.1016/j.jnucmat.2008.08.005.

[27] STEINER P J, BURNS J T. Mechanistic studies of intergranular stress corrosion cracking in Al-Mg alloys under atmospheric exposure conditions [J]. Corrosion, 2018, 74(10): 1117−1131. DOI: 10.5006/2853.

[28] TANGUY D, BAYLE B, DIF R, et al. Hydrogen effects during IGSCC of pure Al-5Mg alloy in NaCl media [J]. Corrosion Science, 2002, 44(6): 1163 − 1175. DOI: 10.1016/S0010-938X(01)00140-8.

[29] MCMAHON M E, HAINES R L, STEINER P J, et al. Beta phase distribution in Al-Mg alloys of varying composition and temper [J]. Corrosion Science, 2020, 169: 108618. DOI: 10.1016/j.corsci.2020.108618.

[30] HIRAYAMA K, TODA H, FU Dong-sheng, et al. Damage micromechanisms of stress corrosion cracking in Al-Mg alloy with high magnesium content [J]. Corrosion Science, 2021, 184: 109343. DOI: 10.1016/j.corsci.2021.109343.

[31] CABRERA-CORREA L, GONZÁLEZ-ROVIRA L, OJEDA-LÓPEZ A, et al. Localized and stress corrosion cracking of sensitized Al-Mg-Sc-Zr alloy manufactured by laser powder bed fusion [J]. Corrosion Science, 2023, 218: 111166. DOI: 10.1016/j.corsci.2023.111166.

[32] M B K, RAJA V S. Hydrogen embrittlement susceptibility of over aged 7010 Al-alloy [J]. Journal of Materials Science, 2006, 41(17): 5495−5499. DOI: 10.1007/s10853-006-0287-1.

[33] SHENG Hai, DONG Chao-fang, XIAO Kui, et al. Localized electrochemical characterization of high strength aluminium alloy at the crack tip in 3.5% NaCl solution [J]. Acta Metallurgica Sinica, 2012, 48(5): 414−419.

[34] LE A H, FOLEY R T. Technical note: On the nature of the occluded cell in the stress corrosion cracking of AA7075-T651: Analysis of the solution inside the crack [J]. Corrosion, 1984, 40(4): 195−197. DOI: 10.5006/1.3581939.

[35] DESHPANDE V S, NEEDLEMAN A, van der GIESSEN E. Discrete dislocation modeling of fatigue crack propagation [J]. Acta Materialia, 2002, 50(4): 831 − 846. DOI: 10.1016/S1359-6454(01)00377-9.

[36] XIE De-gang, LI Su-zhi, LI Meng, et al. Hydrogenated vacancies lock dislocations in aluminium [J]. Nature Communications, 2016, 7: 13341. DOI: 10.1038/ncomms13341.

**(Edited by YANG Hua)**

## 中文导读

# 钨极惰性气体焊Al-Mg-Mn-Sc-Zr合金的应力腐蚀开裂行为

**摘要：**具有优异焊接性能的Al-Mg-Mn-Sc-Zr合金已成为航空航天应用的理想候选材料。目前，对钨极惰性气体(TIG)焊接条件下合金腐蚀行为的研究还不够充分。在此，使用浸泡在3.5% NaCl溶液中的预开裂紧凑拉伸样品，研究了TIG焊接Al-Mg-Mn-Sc-Zr合金的基材(BM)和焊缝区域(WZ)的应力腐蚀开裂(SCC)行为。采用直流电压降(DCPD)法记录裂纹扩展。通过SEM、EBSD和TEM研究了TIG焊接接头不同区域的微观组织及断口形貌，并分析了BM和WZ的SCC裂纹扩展机理。结果表明，BM和WZ的应力腐蚀开裂的临界应力强度因子($K_{ISCC}$)分别为7.05 MPa·m$^{1/2}$和11.79 MPa·m$^{1/2}$。BM应力腐蚀裂纹扩展速率快于WZ，BM比WZ更容易发生SCC。并且，BM区域的断裂方式主要为穿晶断裂，WZ区域的断裂方式主要为沿晶和穿晶混合断裂。此外，应力腐蚀裂纹扩展归因于阳极溶解和氢脆的共同作用。这项研究将为TIG焊接Al-Mg-Mn-Sc-Zr合金在航空航天领域的广泛应用提供实验和理论依据。

**关键词：**钨极惰性气体(TIG)焊接Al-Mg-Mn-Sc-Zr合金；应力腐蚀开裂；临界应力强度因子(SCC)；直流电压降